Effect of dissolved organic matter and its fractions on disinfection by-products formation upon karst surface water

Hui Zhou [a,1], Liye Tian [a,1], Maofei Ni [a,**], Sixi Zhu [a], Runyu Zhang [b], Liying Wang [b], Ming Wang [a], Zhikang Wang [a,*]

[a] *College of Eco-Environmental Engineering, Guizhou Minzu University, Guiyang, 550025, China*
[b] *State Key Laboratory of Environmental Geochemistry, Institute of Geochemistry, Chinese Academy of Sciences, Guiyang, 550009, China*

HIGHLIGHTS

- DBP formation from DOM and its fractions were investigated at karst surface water.
- DOM characteristics responded to spatiotemporal DBPs formation.
- TCM and DCAN formation was significantly higher in drought period than post-wet period.
- Both flushed terrestrial and endogenous organic matter were important DBP precursors.
- Ca^{2+} and Mg^{2+} complexation in AOM affects DBP formation.

GRAPHICAL ABSTRACT
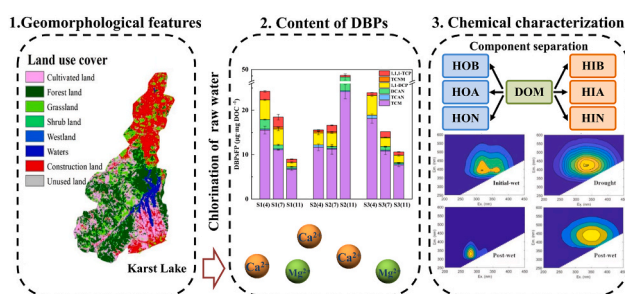
ARTICLE INFO

ABSTRACT

In this study, disinfection by-products (DBP) formation from dissolved organic matter (DOM) and its fractions, including both hydrophilic and hydrophobic components, were investigated at a typical karst surface water. The subsequent DBP formation potential was evaluated by deducing chemical characteristics of DOM fractions and representative algal organic matter (*Chlorella* sp. AOM) under the influence of divalent ions (Ca^{2+} and Mg^{2+}) *via* spectra analysis. Both terrigenous and autochthonous DOM performed as critical DBP precursors, and DBP formation patterns were tightly correlated to organic matter chemical variations. DBP formation was significantly higher in drought period compared to that in wet period (P < 0.05). Particularly, trichloromethane (TCM) and dichloroacetonitrile (DCAN) showed distinct formation patterns compared to the scenarios in non-karst water. For DOM fractions, hydrophobic components showed higher DBP formation compared to hydrophilic counterparts, hydrophilic neutral enriched more reactive organic nitrogen for N-DBPs production. It was preferable to enrich humic-like substances after Ca^{2+} and Mg^{2+} complexation in *Chlorella* sp. AOM, TCM formation increased whereas DCAN production remained unchanged in the presence of divalent ions. This study innovatively provided a linkage between chemical characteristics of DOM and understanding of DBP formation in karst surface water.

* Corresponding author.
** Corresponding author.
   E-mail addresses: nimaofei000@163.com (M. Ni), wangzhikang@gzmu.edu.cn (Z. Wang).
[1] These two authors contributed equally to this work.

1. Introduction

Since 1970, about 800 ubiquitously regulated and emerging disinfection by-products (DBPs) have been detected (Jiang et al., 2020; Yang et al., 2019) and their carcinogenicity and mutagenicity have been widely reported (Han et al., 2021; Hua and Reckhow, 2007a; Li et al., 2020; Richardson et al., 2007; Wagner and Plewa, 2017; Yang and Zhang, 2013). Dissolved organic matter (DOM) is a class of mixed organic molecules (e.g., polysaccharides, proteins and humus) that consists of miscellaneous chemical functional groups, including amino, carboxyl, ester, hydroxyl, ketone and phenol, etc. (Bond et al., 2011; Liang and Singer, 2003; Xu et al., 2021). Natural DOM in aquatic ecosystems shows a multifaceted role and is widely involved in a range of processes, including biological, chemical and physical transformations (Lee et al., 2018).

Lakes and reservoirs are fundamental surface water resources for inland cities. Complicated DOM dynamics would increase difficulties of water treatment operations (Baghoth et al., 2011; Pivokonsky et al., 2015). Natural DOM from terrestrial (e.g., soil-derived organic matter) and endogenous (e.g., algal organic matter, AOM) have been shown to possess complexed organic constituents and abundant reactive moietieis (Gu et al., 2020; Sururi et al., 2020), which could penetrate traditional water treatment processes and result in unwanted production of DBPs during the disinfection process (Chang et al., 2013; Leloup et al., 2013; Pivokonsky et al., 2021). Therefore, it is necessary to further explore the linkage between DOM characteristics and the DBP formation pathway.

Although DBP formation and possible formation mechanisms in freshwater DOM have been investigated (Chang et al., 2013; Xu et al., 2021), the cases of relative studies in karst waters were rarely noticed. Karst landforms account for 15% of the global land area, and cover an area of 3.44 million square kilometers in China (Song et al., 2017). Compared with regular shallow lakes, karst water possesses significantly different geological and geographical background and material circulation characteristics (Zhang et al., 2021). The likelihood of contaminants migrating through topsoil and subsoil or *via* surface karst features (e.g., dolines, swallow holes), cracks and fissures of bedrock can affect DOM property in this vulnerable ecosystem (O'Driscoll et al., 2020; Pavlis and Cummins, 2014).

Trend of eutrophication outbreak and DOM chemical characteristics in karst reservoirs are impelled by the transformation from dissolved inorganic carbon (DIC) to organic components (Bao et al., 2020) through the "biological carbon pump" effect (Chen et al., 2017; Liu and Dreybrodt, 2015). Previous studies have proposed that DIC levels are positively correlated with the production of autochthonous organic carbon through the aquatic photosynthesis effect (Waterson and Canuel, 2008; Yang et al., 2017). This evidence indicates that transformation from DIC to DOM is a notable phenomenon in karst water. In addition, the released Ca^{2+} and Mg^{2+} from dolomite and limestone *via* carbonate dissolution in karst water can also contribute extra substrate for algae growth (Karimova et al., 2000; Pokharel et al., 2018). Algae proliferation, reservoir AOM molecular weight distribution, and secretion of phospholipids can be also altered by Ca^{2+} and Mg^{2+} input (Melcrová et al., 2019; Waditee et al., 2004). Previous studies manifested that the increased level of Ca^{2+} and Mg^{2+} could divert chlorination reaction pathway and respond to the formation of DBPs (Navalon et al., 2009; Zhao et al., 2016). Despite the above-mentioned evidence indicates that both divalent ions and DIC transformed organic carbon alter DBP formation patterns, investigation of DOM properties in karst water and DBP formation research have been unfortunately separated into two areas of study, although significant interaction likely occurs between them.

To better evaluate the role and composition complexity of DOM in aquatic systems, fractionation techniques have been applied to isolate DOM into different fractions, such as hydrophobic, hydrophilic, and neutral components (Aiken et al., 1992; Wang et al., 2009; Zheng et al., 2016). Six regular DOM fractions, including hydrophobic bases (HOB), hydrophobic acidic (HOA), hydrophobic neutral (HON), hydrophilic

bases (HIB), hydrophilic acidic (HIA), and hydrophilic neutral (HIN), are commonly considered as primary components through amberlite XAD resin separation (Leenheer, 1981; Wang et al., 2009). Hydrophobic components conventionally contain high molecular weight of unsaturated functional groups and was traditionally attributed to terrestrial input (Hua and Reckhow, 2007b). Conversely, hydrophilic components traditionally possess low molecular weight molecular amino acids and soluble microbial products (SMP), which was considered as metabolites of microorganisms (Deng et al., 2019). The halogenated active structures, such as aromatic structure, unsaturated carbon and peptide bond, are considered as fundamental halogenated active reaction sties for DBP production (Bond et al., 2011; Gu et al., 2020; Shan et al., 2012). In addition, spatiotemporal variability of DOM affected by allochthonous and autochthonous sources also cause diverse chlorination reactivity (Liu et al., 2018; Ni et al., 2020; Xu et al., 2021). Despite the fact regarding contributions from DOM to DBP formation and their potential health risks have undergone considerable scrutiny, there is still a lack of comprehensive information about the impact of spatiotemporal DOM patterns on DBP formation in karst water. Accordingly, evaluating DBP formation from chemical characterization and spatiotemporal approaches may provide a more fundamental understanding toward internal links of DOM-DBP formation in karst water.

This study aims to elucidate the response of DBP formation to DOM characteristics and fractions in the karst water. We thus examined water quality characteristics, DOM optical properties, DOM fractions (HOB, HOA, HON, HIB, HIA and HIN), representative AOM extracted from *Chlorella* sp., and their subsequent DBPs formation potential (DBPsFP) in a representative karst surface water (the Aha Reservoir). Characteristics of these organic matters were deduced by Ultraviolet–visible (UV–Vis) absorption, three-dimensional Excitation and Emission (3D-EEM) and Fourier transform infrared (FTIR) techniques. Formation potential of carbonaceous DBPs (C-DBPs) and nitrogenous DBPs (N-DBPs) was examined considering three typical locations, sampling periods and the influence of Ca^{2+} and Mg^{2+}. Our results are expected to supplement the knowledge gap of DOM chemical characteristics and DBP formation control in this vulnerable aquatic ecosystem.

2. Materials and methods

2.1. Sampling site information

The Aha Reservoir, one of the main local drinking water sources, is located in a typical karst area, Guiyang, Guizhou Province, in the southwest of China (26°32′ - 26.67″N and 106°38′ - 51.27″E, Fig. 1). The detailed information of Aha Reservoir can be found in Supplementary Information (SI 1). Water samples were obtained in November 2018 (drought period), April 2019 (initial-wet period), and July 2019 (post-wet period). The sampling points include two river estuaries (#S1 and #S3) and a drinking water intake (sampling point, #S2). In detail, the estuary of the Jinzhong River (sampling point, #S1) carries the domestic sewage input from the uptown (Guanshanhu District) of Guiyang, suggesting anthropogenic organic matter entered in this water area. The estuary of the Youyu River (sampling point, #S3) has been affected for decades by the input of acid coal mine wastewater from the mining area of Jiu'an County (Huaxi District). Excessive Ca(OH)$_2$ was dosed for acidic water treatment (neutralization) that may cause the increase of Ca^{2+} level at this location.

2.2. Sample collection and preservation

All samples were collected 0.5 m below the water surface, then stored in 1000 mL high-density polyethylene (HDPE) plastic containers (avoiding organic matter absorption by the material surface) for subsequent laboratory analysis (Ni et al., 2022; Yuan et al., 2013). To obtain dissolved organic carbon (DOC), 0.45 μm cellulose acetate (CA) membranes (GF/F 47 mm, Whatman, USA) were used for sample filtration.

Filtrate for DOC determination was acidified to pH < 2 with concentrated H_2SO_4 to avoid sample deterioration.

Water temperature, pH, and dissolved oxygen (DO) were measured *in-situ* by potable multifunctional water quality parameter instruments (pHB-4 and JPB-607A, Leici, China). The secchi disk depth (SDD) was measured with a Secchi disk (SD-20, Beijing, China). Aqueous Ca^{2+} and Mg^{2+} levels were determined by EDTA titration method (Holroyde et al., 1980). The UV–Vis spectrophotometric method was employed for the analysis of total phosphorus (TP) and Chlorophyll *a* (Chla) concentrations: (i) TP was determined with ammonium molybdophosphate colorimetry (Lu et al., 2011), and (ii) Chla was extracted by ethanol (Pápista et al., 2002). DOC, DIC, and total nitrogen (TN) were measured by a vario/select total organic carbon analyzer (Elementar, Germany) with a TN analysis unit.

2.3. Resin pretreatment and DOM fraction

All resins were carefully cleaned before use to avoid any chemical interfere. The detailed steps are summarized in SI 2. The DOM fractions detachment was conducted based on the previous methods provided by Leenheer (1981) and Wang et al. (2009) as shown in SI 3. Approximately 1400 mL of raw water DOM was separated into six fractions: HOB, HOA, HON, HIB, HIA and HIN. The elution and adsorption flow rates were 2.5 and 5 mL min^{-1}, respectively.

2.4. DOM chemical characterization

2.4.1. UV–vis

UV–Vis can determine specific functional groups-enriched DOM at the corresponding wavelengths (Li et al., 2014; Omanović et al., 2019). For instance, UV$_{254}$, UV$_{280}$, and UV$_{285}$ can be used for characterizing aromatic (Kida et al., 2018), protein (Fichot and Benner, 2012), fulvic acid organic matter (Piirsoo et al., 2012), respectively. Spectral slopes ($S_{275-295}$, $S_{290-350}$ and $S_{350-400}$) and their ratio ($S_{R=S_{275-295}/S_{350-400}}$) represent relative DOM molecular weight distribution (Liu et al., 2018; Ni et al., 2020; Shank and Evans, 2011). Original DOM and six fractionated components were scanned by a UV–Vis analyzer (UV 1800, Meixi, China) within 200–700 nm, and the blank was deducted with deionized (DI) water (18.2 MΩ cm). The specific absorbances at 254 nm, 280 nm and 285 nm were recorded. The spectral slope ($S_{275-295}$) was calculated by nonlinear fitting of the exponential function of the absorption spectrum at wavelengths from 275 to 295 nm.

2.4.2. FTIR analysis

FTIR is used to identify DOM chemical functional groups and components. Original DOM and six fractionated components were filtered and hydrolyzed in a vacuum freeze dryer (LGJ-12T, Songyuanhuaxin, China) at four temperature gradients (20–0, 0 ~ −10, −10 ~ −60 and −60–0 °C). After the freeze-drying process, samples and KBr (spectral pure, Aladdin Co., Shanghai) were mixed and compressed by a tablet machine (HY-12, Tianjing, China), and the FTIR of samples were characterized on an infrared spectrometer (Nicolet 6700, Thermo, USA).

2.4.3. 3D-EEM and parallel factor (PARAFAC) analysis

3D-EEM spectroscopy technique was issued to identify specific DOM components (Chen et al., 2003; Kida et al., 2019). Original DOM and six fractionated components were characterized by 3D-EEM spectroscopy. All samples were diluted by DI water, and prepared KCl stock solution was added into samples to make its background concentration of 0.01 mol L^{-1}. Three-dimensional scanning was carried out by a fluorescence spectrophotometer (F-380, Gangdong, China). Excitation (*Ex*) wavelength was set from 200 to 450 nm (interval 5.0 nm) and emission (*Em*)
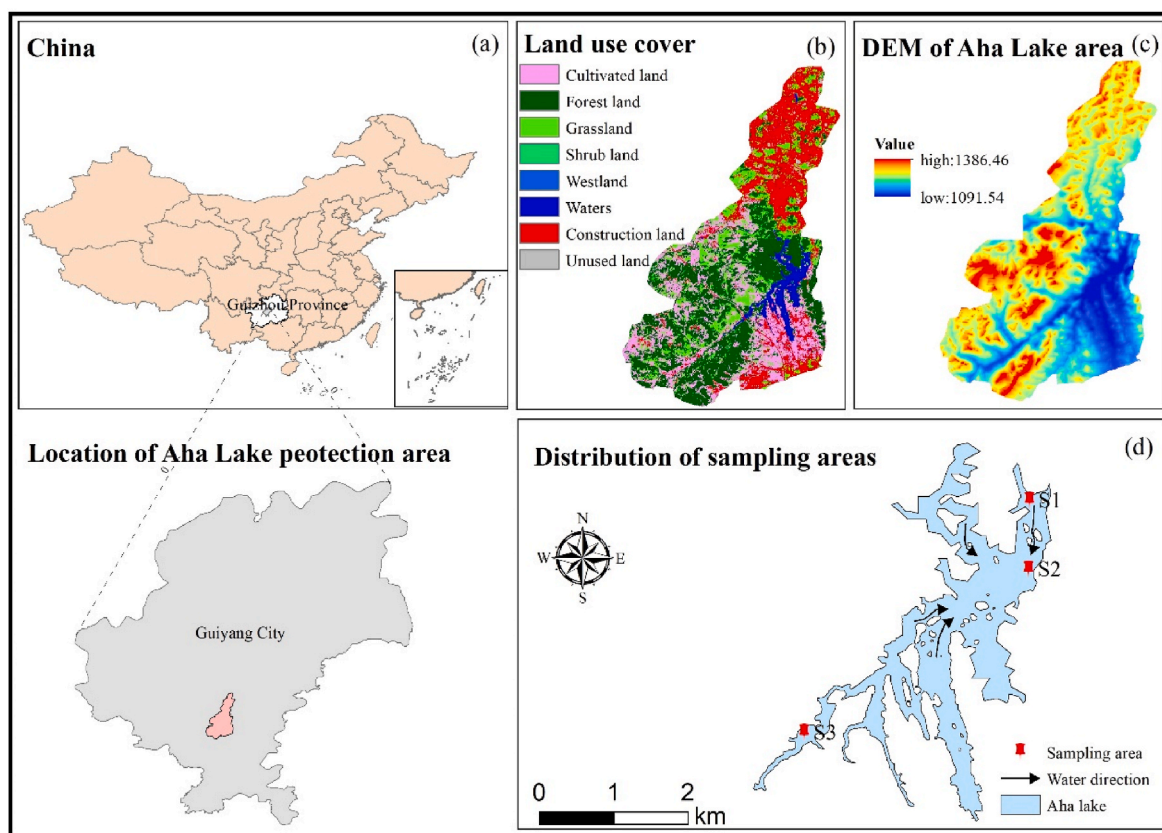

Fig. 1. Geographical local and sampling information (a. Location of Aha reservoir; b. DEM of the reservoir catchment; c. Land use cover of the reservoir catchment; d. Distribution of sampling areas) of Aha reservoir, Guiyang, Southwest China (#S1, the estuary of Jinzhong river; #S2, drinking water intake of Aha reservoir; #S3, estuary of Youyu river).

wavelength was set from 250 to 600 nm (interval 1.0 nm). Scanning speed, slit width and voltage were set to be 2400 nm min^{-1}, 5.0 nm and 700 V, respectively. During 3D-EEMPARAFAC analysis, the blank was deducted and the interference peak was omitted. The appropriate model for DOM components was verified with split half analysis by using MATLAB 2018a (MathWorks, Natick, MA) in a DOMFluorv 1.71 toolbox (Tedetti et al., 2012). Further details can be found elsewhere in the operational protocol (Stedmon and Bro, 2008).

2.5. DBPsFP test

The DBPsFP tests were conducted through DOM obtained from sampling sites #S1~#S3, and the subsequent DOM fractions including both three hydrophilic (HIA, HIN, HIB) and hydrophobic components (HOA, HON, HOB). Samples were loaded in a series of 40 mL amber glass vials with phosphate buffer (pH = 7), then exposed to excessive Cl$_2$ doses (~20:1 mg Cl$_2$/mg DOC) following the standard method 5710B (Baird et al., 2017) and incubated in the dark at room temperature (22 ± 2 °C) for three days (Wang et al., 2012b). Both volatile C-DBPs (e.g., trichloromethane (TCM), 1,1-dichloropropanone (1,1-DCP) and 1,1, 1-trichloropropanone (1,1,1-TCP)) and N-DBPs (e.g., dichloroacetonitrile (DCAN), trichloroacetonitrile (TCAN) and trichloronitromethane (TCNM)) were analyzed by a gas chromatography with electron capture detector (GC-ECD, trace GC 1300, Thermo Scientific, USA). The GC column was TG-5MS (30 m × 0.32 mm × 0.25 μm). The 99.999% purity of carrier gas (N$_2$) flow was 1 mL min^{-1}, the temperature of the injection port was set at 200 °C, and the temperature of the ECD detector was set at 300 °C. The specific temperature program procedures: maintain at 35 °C for 9 min and rise to 40 °C (for 1 min) at the rate of 2 °C min^{-1}, then rise to 80 °C at the rate of 20 °C min^{-1}, and finally rise to 160 °C (for 4 min) at the rate of 40 °C min^{-1}. The recoveries of all DBPs tested in the experiment ranged within 80.0%–120.0%, and the method detection limit of all tested DBPs was at ~ 0.1 μg L^{-1}. DBPsFP were calculated based on the formation per organic carbon contribution (μg mgDOC^{-1}).

2.6. Effect of Ca^{2+} and Mg^{2+}

To identify the influence of divalent ions (Ca^{2+} and Mg^{2+}) on DBP formation, spectra characteristics and DBPsFP were conducted by selected AOM, one of the dominant algal species (*Chlorella* sp.) in Aha Reservoir. The modified BG11 medium (Table S1) was configured to simulate regional karst conditions for *Chlorella* sp. Cultivation. After the cell concentration reached at 3 × 10^6 cells mL^{-1} (stationary phase), the medium was decanted by centrifugation (2000 r min^{-1}) and washed

twice by DI water. After that, AOM was obtained according to the protocol of Wang et al. (2021). Two divalent ion concentration gradients (Ca^{2+} = 135.71 mg L^{-1}, Mg^{2+} = 18.43 mg L^{-1}; Ca^{2+} = 60.74 mg L^{-1}, Mg^{2+} = 15.46 mg L^{-1}) detected in surface water of sampling sites (Table 1) were blended with AOM (TOC = ~3 mg L^{-1}) for 1 h by magnetic stirring. AOM with divalent ion addition and control groups were further conducted by UV–Vis, 3D-EEM, and DBPsFP experiments with the procedures mentioned at sections of 2.4.1, 2.4.3, and 2.5, respectively. All samples were analyzed in duplicate for calculating standard deviation. Data processing was conducted by Origin pro 2018 (USA). Statistical differences and correlations were calculated by SPSS 26 (IBM, USA).

3. Results and discussion

3.1. Water quality characteristics

The water quality parameters at Aha Reservoir during three sampling periods are shown in Table 1. In general, pH (7.29–8.64) was found within the normal range in karst water (Longyang, 2019), and DO (6.0–18.8 mg L^{-1}) was oversaturated (Ge et al., 2021). Typical karst water characteristic was reflected by 22.92–36.33 mg L^{-1} of DIC levels across periods, which were much higher compared to those in non-karst water. The DOC levels ranged from 2.01 to 4.09 mg L^{-1}, with the highest level (4.09 ± 0.15 mg L^{-1}, mean ± standard deviation, the same as below) at #S2 in post-wet period. The average DOC in post-wet period (2.83–4.09 mg L^{-1}) was higher than those in the initial-wet (2.01–3.39 mg L^{-1}) and drought periods (2.07–2.96 mg L^{-1}) (P < 0.05). Chla levels showed significant variations in different sampling locations (P < 0.01), ranging from 1.99 to 131.69 μg L^{-1}, with an average of 49.80 μg L^{-1}. The levels of Chla in the initial-wet and post-wet periods at #S1 (119.97–131.69 μg L^{-1}) and #S2 (76.45–74.21 μg L^{-1}) were much higher than that in #S3 (6.70–21.76 μg L^{-1}). The increased TN (2.02–4.09 mg L^{-1}) and TP (0.011–0.171 mg L^{-1}) levels at the initial-wet and post-wet periods may cause eutrophication outbreak and subsequently impact DOM chemical composition (Bao et al., 2020).

Parameters including Chla, DOC and TN also demonstrated evidence that algal growth mainly occurred during wet periods. This was consistent with high trophic state index (TSI) in Aha Reservoir (Ni et al., 2021): Eutrophication (TSI > 50) in the initial-wet period and meso-trophication (30 < TSI < 50) in the post-wet period (SI 5). Intriguingly, Chla levels in #S2 (1.99 ± 0.27 μg L^{-1}) were decreased by 58.4% and 80.8% compared to #S1 (4.78 ± 0.47 μg L^{-1}) and #S3 (10.36 ± 0.28 μg L^{-1}) during the drought period, while DOC levels increased by 7.4% and

Table 1
Spatiotemporal analysis of water quality characteristics in Aha reservoir.

	#S1			#S2			#S3		
	initial-wet	post-wet	drought	initial-wet	post-wet	Drought	initial-wet	post-wet	drought
Temperature (°C)	19.7 ± 0.3^D	28.8 ± 0.6^A	16.5 ± 0.3^F	19.8 ± 0.3^D	27.1 ± 0.4^B	16.3 ± 0.2^F	22.9 ± 0.7^C	27.2 ± 0.4^B	18.0 ± 0.4^E
pH	8.64 ± 0.01^A	8.47 ± 0.02^C	7.71 ± 0.01^E	8.63 ± 0.02^{AB}	8.60 ± 0.01^B	7.68 ± 0.01^E	7.82 ± 0.02^D	8.60 ± 0.01^B	7.29 ± 0.03^F
DO (mg L^{-1})	18.8 ± 0.2^A	8.2 ± 0.1^E	6.2 ± 0.3^F	18.5 ± 0.3^A	9.8 ± 0.3^C	6.0 ± 0.1^F	8.9 ± 0.2^D	11.5 ± 0.2^B	9.2 ± 0.1^{CD}
TP (mg L^{-1})	0.171 ± 0.001^A	0.162 ± 0.002^B	0.081 ± 0.001^C	0.061 ± 0.001^E	0.082 ± 0.002^C	0.073 ± 0.002^D	0.012 ± 0.001^F	0.013 ± 0.001^F	0.011 ± 0.001^F
TN (mg L^{-1})	3.73 ± 0.04^B	4.09 ± 0.03^A	2.28 ± 0.03^F	2.38 ± 0.03^E	3.49 ± 0.07^C	2.69 ± 0.05^B	2.12 ± 0.03^G	2.60 ± 0.01^D	2.02 ± 0.02^H
DOC (mg L^{-1})	3.39 ± 0.26^B	3.53 ± 0.09^B	2.74 ± 0.10^{CD}	2.01 ± 0.06^E	4.09 ± 0.15^A	2.96 ± 0.02^C	2.48 ± 0.09^D	2.83 ± 0.01^C	2.07 ± 0.03^E
DIC (mg L^{-1})	28.27 ± 0.83^D	29.36 ± 0.65^{CD}	30.37 ± 0.06^C	28.96 ± 0.86^D	26.71 ± 0.33^E	33.11 ± 0.13^B	36.33 ± 0.12^A	22.92 ± 0.33^F	32.59 ± 0.60^B
Chla (μg L^{-1})	119.97 ± 0.39^B	131.69 ± 0.19^A	4.78 ± 0.47^H	76.45 ± 0.53^C	74.21 ± 0.92^D	1.99 ± 0.27^I	6.70 ± 0.39^G	21.76 ± 0.94^E	10.36 ± 0.28^F
Ca^{2+} (mg L^{-1})	63.45 ± 0.07^F	61.16 ± 0.59^G	88.58 ± 0.19^C	71.78 ± 0.21^D	65.25 ± 0.11^E	89.38 ± 0.17^C	135.35 ± 0.51^A	72.14 ± 0.25^D	98.84 ± 0.53^B
Mg^{2+} (mg L^{-1})	17.46 ± 0.01^B	16.09 ± 0.08^D	16.73 ± 0.12^C	17.59 ± 0.08^B	15.47 ± 0.01^E	17.43 ± 016^B	18.18 ± 0.16^A	15.81 ± 0.23^{ED}	18.26 ± 0.25^A

Significance Level: 0.01. N = 3.

30.1%, respectively. Chla was probably degraded by exposure to strong sunlight from July to October (Cuny et al., 2002; Hansen et al., 2016). Furthermore, relatively small organic molecules of alga detritus in the euphotic layer were produced, which was deduced by the decreased Chla and concomitant increased DOC.

The level of Ca^{2+} (61.16–135.35 mg L^{-1}) was much higher than that of Mg^{2+} (15.47–18.26 mg L^{-1}), the treatment of acid coal mine wastewater by adding $Ca(OH)_2$ upstream in Youyu River might lead to the highest Ca^{2+} levels at #S3 (102.11 ± 31.73 mg L^{-1}) compared to those of #S1 (71.06 ± 15.21 mg L^{-1}) and #S2 (75.47 ± 12.48 mg L^{-1}). The presence of Ca^{2+} and Mg^{2+} can compress electric double layer and reduce the potential energy of DOM *via* bridging effect by connecting divalent ion and certain negative functional groups (e.g. –COOH and –OH) (Wang et al., 2012a; Xu et al., 2019). Besides, excessive Ca^{2+} might inhibit algae growth (Melcrová et al., 2019) and alter AOM chemical composition. Significant negative correlation between Ca^{2+} and Chla (R = −0.921 ~ −0.999) (P < 0.01) was observed (Table S3), which documented that Ca^{2+} posed a negative exert on algae reproduction in karst water. In comparison to the effect of divalent ion, the pronounced increase of Chla (P < 0.01) at the anthropogenic-related site (#S1) showed a marginal impact on the variety of aromatic and protein-like substances, despite the linked Chla and DOC (P < 0.01) suggests enriched AOM at #S1 (Table S4). Accordingly, the presence of Ca^{2+} and Mg^{2+} may perform a critical influential factor for DOM variations.

3.2. The chemical characterization of DOM and its fraction

3.2.1. UV–Vis

The temporal and spatial changes of SUVA254, SUVA280, SUVA285 and S_R values of #S1~#S3 are shown in Fig. 2. SUVA254 (aromaticity index) showed a downward trend from the initial-wet and post-wet periods to the drought period. For instance, SUVA254 at #S1 showed a decreased trend from 2.87 ± 0.008 to 0.39 ± 0.007 L mg^{-1} m^{-1}. A similar trend was observed at #S2 (from 3.39 ± 0.003 to 0.19 ± 0.002 L mg^{-1} m^{-1}) from the initial-wet period to the drought period. For #S3, extremely high SUVA254 (3.59 ± 0.41 L mg^{-1} m^{-1}) was found in the initial-wet period compared to the post-wet and drought periods (P < 0.05). Similarly, SUVA280 (protein index) showed an identical trend when compared to SUVA254, suggesting a strong correlation between aromaticity and protein (Liu et al., 2018; Wang et al., 2013). Strikingly, the SUVA254 and SUVA280 at #S3 were much lower (85.0%–87.0%) compared to #S1 and #S2 at the post-wet period (P < 0.05). However, SUVA285 (fulvic acid index) showed distinctive patterns, which reached a maximum (2.67 ± 0.30 L mg^{-1} m^{-1}) in the initial-wet period compared to the post-wet (0.17 ± 0.002 L mg^{-1} m^{-1}) and drought (0.40 ± 0.001 L mg^{-1} m^{-1}) periods.

The S_R values are greater than 1 (Fig. 2d), suggesting DOM was prone to be affected by endogenous input (Helms et al., 2008). Meanwhile, the prevalence of allochthonous DOM constituents followed the order of post-wet > initial-wet and drought period based on S_R value. Specifically, SUVA254 (aromatic) and SUVA280 (fulvic acids) of HOA were significantly higher than other DOM fractions (P < 0.01), whereas $S_{275-295}$ values were statistically insignificant across six fractions (P > 0.01, Table S6). This suggested an inapparent molecular weight distribution (Shank and Evans, 2011). In comparison to a karst catchment, Lake Hongfeng, size exclusion chromatography revealed that aquatic DOM and its fractions possessed low molecular weight range (< 3000 Da) (Wang et al., 2009; Zhang et al., 2021). SUVA254, SUVA280 and SUVA285 were remarkably decreased at #S3 at the initial-wet and post-wet periods (P < 0.05), which probably attributed to increased rainfall, runoff and flow in the Youyu River and continuously brought divalent ions from dosed $Ca(OH)_2$. Notably, aquatic Ca^{2+} could positively and negatively correlated to SUVA254, SUVA280, and SUVA285 at

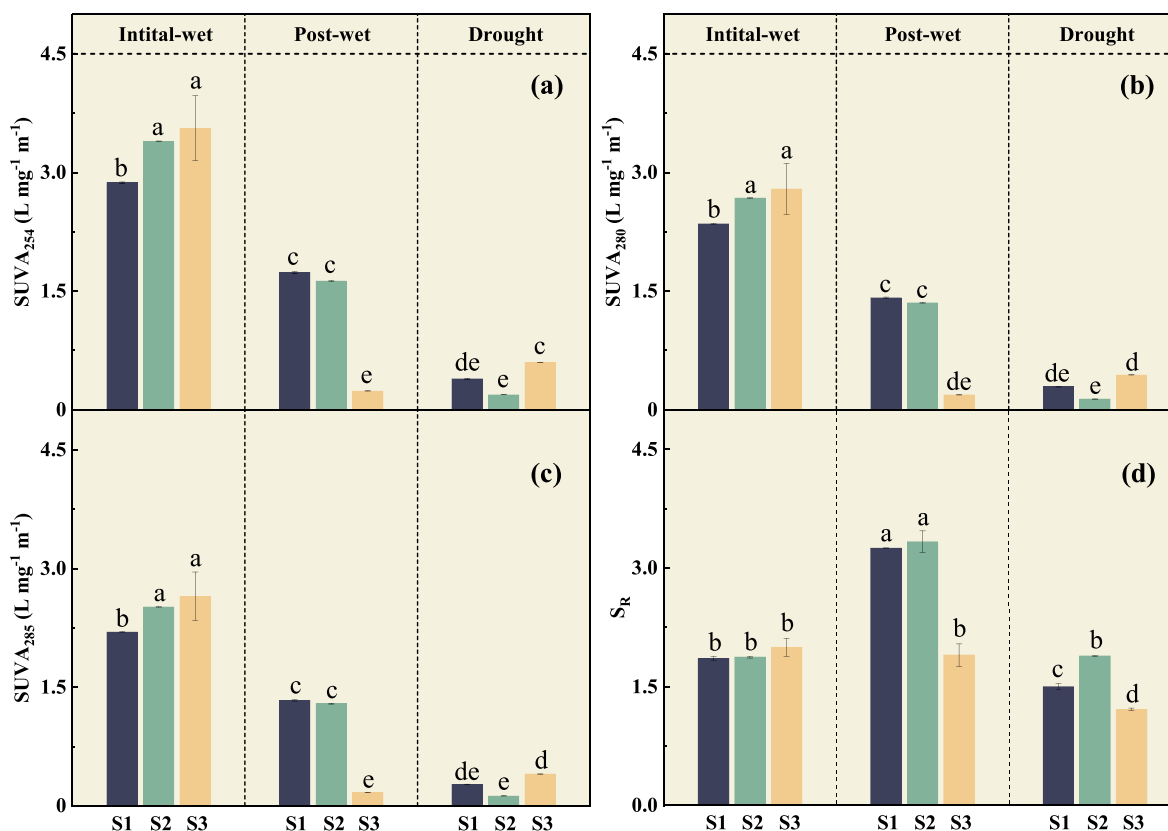**Fig. 2.** The spatiotemporal patterns of DOM absorption coefficients (a. SUVA254; b. SUVA280; c. SUVA285 and d.S_R values) in Aha reservoir; #S1, the estuary of Jinzhong river; #S2, drinking water intake of Aha reservoir; #S3, estuary of Youyu river, the r^2 values of S_R were all over 0.9 (significance level: 0.05, N = 2).

#S1 (R = −0.851 ~ −0.857) (P < 0.05) and #S3 (R = 0.951–0.957) (P < 0.01), respectively (Table S3).

3.2.2. 3D-EEM PARAFAC

The 3D-EEM-PARAFAC analysis of DOM and its fractions are shown in Fig. 3 and Fig. S2, respectively. Overall, two distinctive signal peaks were observed in the post-wet period, while unique peaks were found in the initial-wet and drought periods. In Fig. 3, the humic-fulvic like allochthonous organic substances were identified in both initial-wet and drought periods (Xu et al., 2021). In addition, SMP (Chen et al., 2003) and humic-like components (Wang et al., 2017) were also found in the drought period, due to its wide peak-signal coverage at Ex = 230–480 nm and Em = 310–580 nm. Two distinctive DOM in the post-wet period referred to soluble microbial and humic/fulvic-like products, suggesting algal proliferation and terrestrial humic/fulvic substance inputs.

For DOM fractions (Fig. S2), two components were defined in HIB and one component was identified in other five fractions. From Fig. S2a, b and c, it can be extrapolated that fluorescence peaks of hydrophobic components (HOB, HOA and HON) showed humic/fulvic-like substance signal and peaked at Ex/Em = 340(355)/390(395, 415) nm, with the highest maximum fluorescent intensity in HON (Fig. S2h). For hydrophilic components, soluble microproduct substances were found in HIB and HIN. In addition, humic/fulvic-like substance were also discovered in HIA and HIB. Especially, HIB is mostly attributed to microbial metabolic by-products at Ex/Em = 320–345/370–275 nm and humic acid at Ex/Em = 350/400 nm (Fig. S2e,f). In addition, the primary substances of hydrophobic components in DOM fractions were humic/fulvic substances, whereas hydrophilic components contained both humic/fulvic substances and SMP with unsaturated carbon and organic nitrogen (Fig. S2 and Fig. S4).

3.2.3. FTIR

FTIR spectrums of DOM and its fractions are shown in Fig. S3 and Fig. S4. The characteristic peaks including –CH, –CO, –C≡C—, –C≡C—, –OH and –NH₂ contributed to the main functional groups. In Fig. S3, obvious absorbances in the range from 675–900 cm^{-1}, 1000–1300 cm^{-1} and 1400–1410 cm^{-1} suggested the presence of –CH and –CO. In addition, 1600–1700 cm^{-1} absorbance can be classified as the –C≡C— stretch vibration. Absorbance at 1650 cm^{-1}, 1537 cm^{-1}, and 1240 cm^{-1} respectively belong to the amide I, amide II, and amide III bands, indicating protein-like substance in each DOM component. For DOM fractions, hydrophobic DOM possessed more unsaturated carbon contents compared to hydrophilic DOM (Fig. S4). Strong absorbance was observed at 3300 cm^{-1} as hydroxyl vibration for all DOM fractions that likely belongs to phenolic structure. Specifically, HIB manifested

stronger vibration of unsaturated carbon for –C≡C— and –C≡C— at 1600–1700 cm^{-1} and 2400–2500 cm^{-1}, respectively. However, we did not observe different absorbance intensity for carbohydrate and protein regions in HIA, HIN and hydrophobic components, which suggests an increased proportion of protein-like components.

3.3. DBPsFP of DOM and its fractions

The DBPsFP of DOM at #S1 ~ #S3 in three periods is shown in Fig. 4. Overall, DBPsFP in the post-wet period was significantly lower than those in the initial-wet and drought period (P < 0.01, Table S5). TCM formation potential was found in the range of 6.66–24.16 μg mgDOC^{-1}. For haloketones (HKs), 1,1-DCP formation potential was higher than 1,1,1-TCP. DCAN is the primary formed N-DBP compared to TCAN and TCNM. For spatiotemporal variations, the highest TCM formation potential was discovered at #S2 in the drought period (P < 0.05, Fig. 2b). Additionally, TCM formation potential #S3 was higher than those of #S1 and #S2 at initial-wet period, but no significant differences were observed in the post-wet period (P > 0.05). For HKs, 1,1-DCP formation potentials showed downward trend from initial-wet to post-wet and drought periods, with the highest average level at #S1 (3.01 ± 1.80 μg mgDOC^{-1}). For 1,1,1-TCP formation potential, average levels at #S1 and #S2 were higher than #S3. For N-DBPs, an extremely high DCAN formation potential (19.88 ± 2.35 μg mgDOC^{-1}) was found at #S2 in the drought period (P < 0.05). At the initial-wet period, DCAN formation was solely found at #S1 (2.13 ± 0.10 μg mgDOC^{-1}). Less TCAN and TCNM were found during all sampling sites and periods compared to other tested DBPs.

Elevated temperature can promote DBPs production and increase the rate of algal growth, subsequent chlorine demand, and reaction rate of chlorination (Xu et al., 2021; Zhou et al., 2019). Besides, previous studies also posited that terrestrial DOM is preferable to contribute extra TCM and DCAN formation during the rainy season (O'Driscoll et al., 2020; Xu et al., 2021). O'Driscoll et al. (2020) investigated DBP formation in karst groundwater in Ireland, suggesting terrestrial organic matter was responsible for TCM formation. Aromatic and phenolic substances enriched in AOM and its metabolite in karst water. Meanwhile, tyrosine, phenylalanine and tryptophan were considered as potential TCM precursor as well (Goslan et al., 2017; Hua and Reckhow, 2007b). Surprisingly, it is noteworthy that DBP formation was significantly lower in the post-wet period (P < 0.05) compared to those in the initial-wet and drought periods (Fig. 4 and Table S5). Furthermore, TCM and DCAN formation patterns were not discernible (P > 0.05) during the post-wet period across three sampling sites. The possible explanation is the increased reactive moieties from flushed terrestrial DOM.
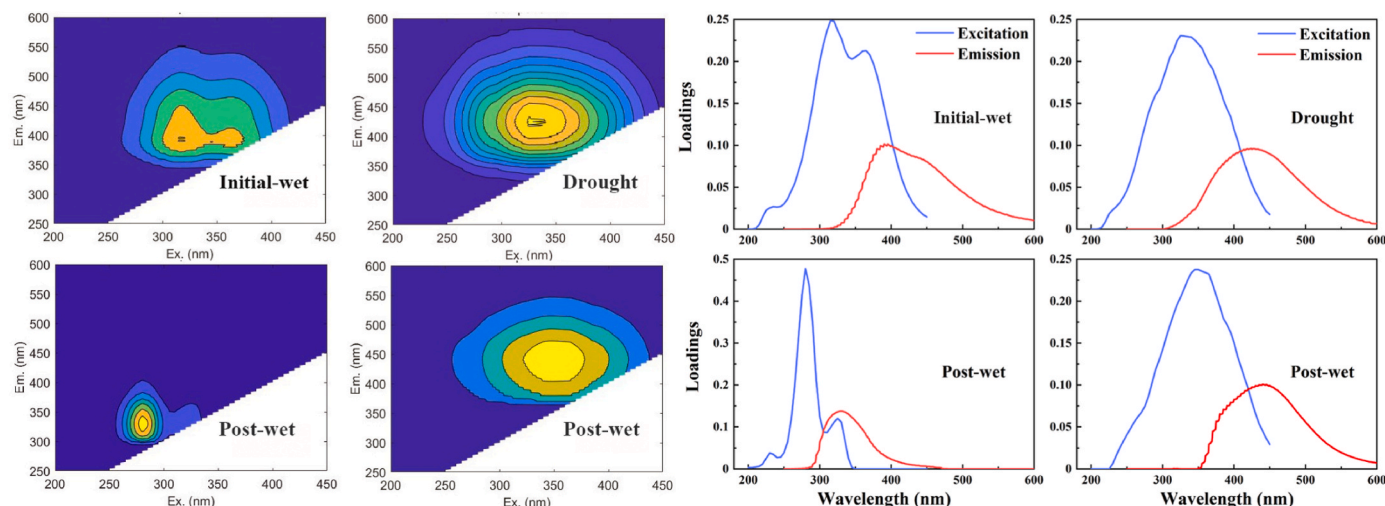

Fig. 3. Fluorescence spectral characteristics of DOM and its excitation and emission loads in three periods of Aha reservoir.
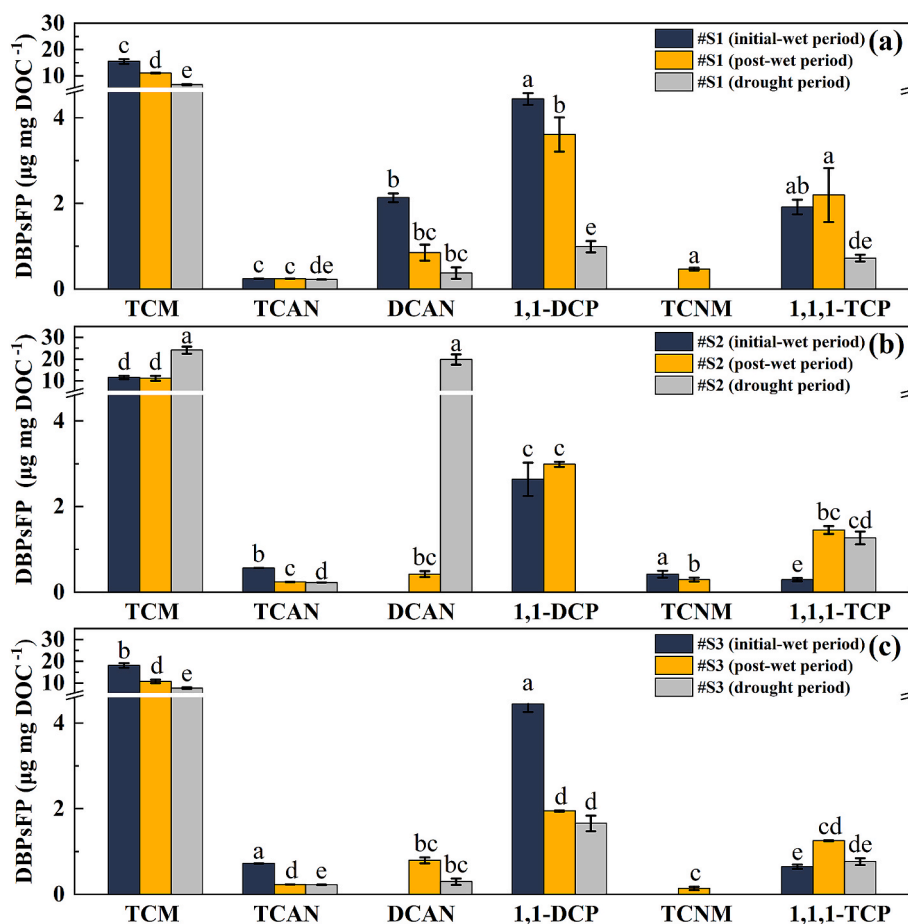
Fig. 4. The DBPsFP of DOM upon chlorination in Aha reservoir during three periods. April (4): initial-wet period; July (7): post-wet period; November (11): drought period. Error bar represents duplicate samples. #S1: the estuary of Jinzhong river; #S2: drinking water intake of Aha reservoir; #S3: estuary of Youyu river (Significance level: 0.05, N = 2).

Interestingly, enhanced TCM and DCAN formation was discovered under the diminishing of terrigenous DOM input in water catchment during the drought period (P < 0.05, Fig. 4b). Overproduction of aromatic protein, tyrosine and tryptophan-like substances were probably the consequence of increased DBP formation (Bond et al., 2011; Goslan et al., 2017; Wang et al., 2013). TSI analysis (Table S2) also confirmed that eutrophication occurred in the drought period, despite previous studies clearly indicated that organic nitrogen enriched in AOM was the primary N-DBP precursor from algal bloom outbreaks during summer in non-karst surface water (Goslan et al., 2017; Li et al., 2020). Besides the influence of temperature, DIC dissolution could be assimilated as nutrients, promoting the growth and outbreak of planktonic algae in karst water (Bao et al., 2020). Accordingly, autochthonous DOM also served as a primary TCM and DCAN precursor.

The DBPsFP of DOM fractions at initial-wet period are shown in Fig. 5. DOM hydrophobic components (HOB, HOA and HON) showed higher DBPsFP compared to its hydrophilic counterparts (HIB, HIA and HIN). Among all tested DBPs, TCM manifested the highest formation potential and possessed temporal and spatial changes, especially for hydrophobic components. In details, TCM formed from hydrophobic components were 178.97 ± 161.45, 134.21 ± 128.96 and 122.49 ± 117.67 µg mgDOC^{-1} for #S1, #S2 and #S3, respectively. Meanwhile, the TCM formation potential pattern changed remarkably during different periods (P < 0.05). At the initial-wet period (Fig. 5), TCM formation from HON accounted for 60.7%–78.2% of total DBPsFP. For the post-wet period (Fig. S5), TCM from HOA was significantly higher (P < 0.05) than that of HON at #S1, and accounted for 53.7% and 48.2% of total DBPsFP at #S1 and #S3, respectively. In the drought period

(Fig. S6), HON was also considered as the major precursor for TCM, accounting for 69.1%–77.6% of total DBPsFP, but TCM formation potential at #S2 was lower than that of #S1 and #S3 (P < 0.05, Table S7).

For HKs, 1,1-DCP and 1,1,1-TCP were mainly contributed by HOB, HON, HOA and HIN, and their formation potentials changed dramatically across periods (P < 0.05). In details, formation potential of 1,1-DCP was mainly contributed by HOB, which accounted for 77.9%, 50.5% and 55.7% of total 1,1-DCP formation potentials in the initial-wet, post-wet and drought periods, respectively. While 1,1,1-TCP was mainly derived from HON, accounting for 92.4%, 75.3% and 97.1% of total 1,1,1-TCP formation potentials in the initial-wet, post-wet and drought periods, respectively.

For N-DBP formation, the average of DCAN formation potential of six DOM fractions was much higher than TCAN formation potential. Primary DCAN precursors were HON, HOA, HOB and HIN. Specifically, HON contributed ~45.5% of DCAN formation potential to DOM fractions. For TCAN, HIA manifested the highest formation potential accounting for ~24.5% in all DOM fractions. In addition, HON and HOA expressed the highest DCAN formation potential during the drought period (Table S7), respectively. For TCNM, HOA showed 0.24 ± 0.03 and 0.57 ± 0.07 µg mgDOC^{-1} TCNM formation potential at #S2 and #S3 in the post-wet period, respectively (Fig. S5). In the drought period, HOA and HOB showed discernible TCNM formation at #S2, which were 0.18 ± 0.11 and 0.08 µg mgDOC^{-1}, respectively.

Although HON may possess less SMP compared to HOA, stronger fluorescence index (FI, Fig. S2h) manifested that fulvic acid-like substance was the primary DBP precursors for HOA (Table S7). For hydrophilic components, HIB showed the feedback of both discernible
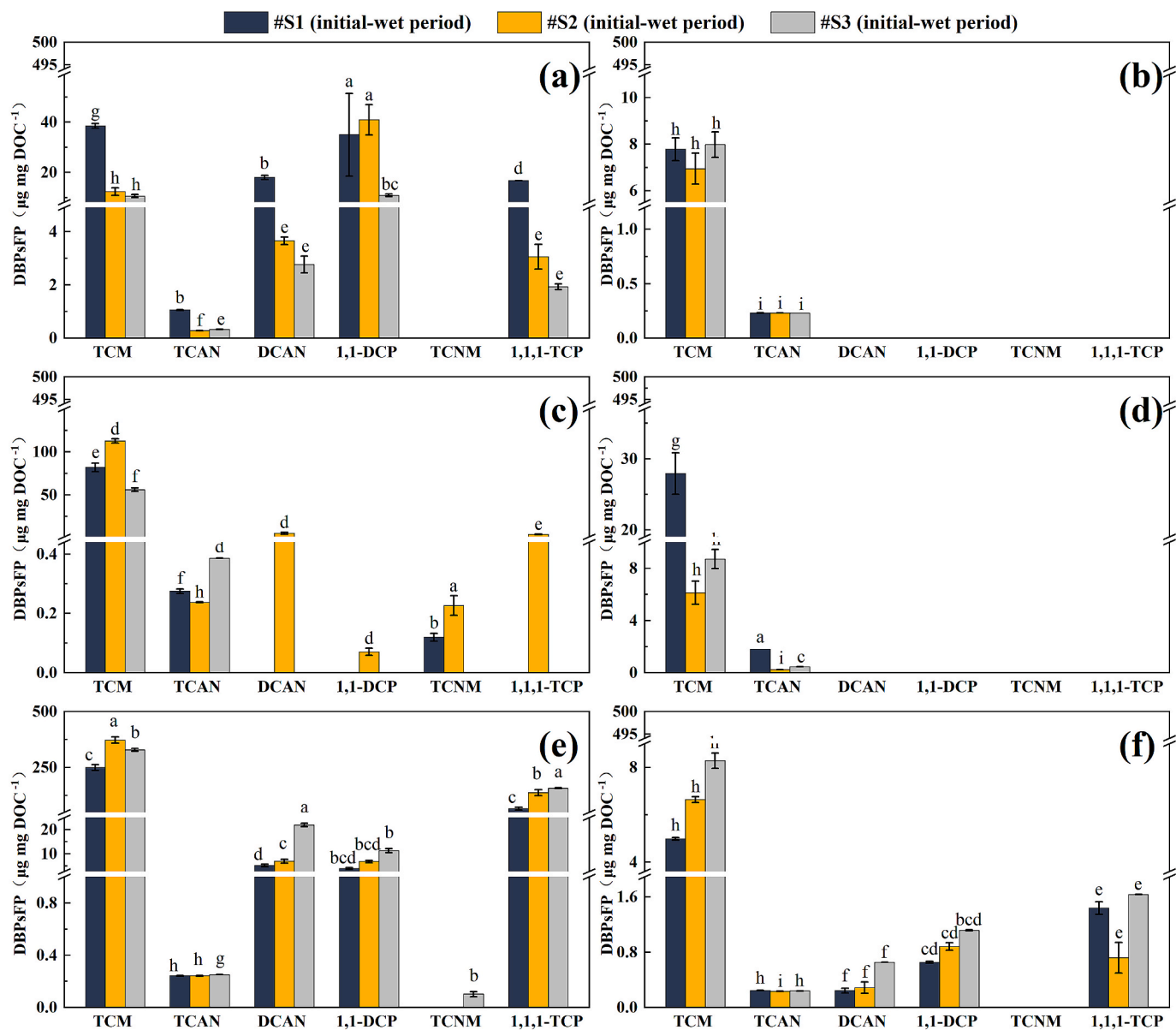
Fig. 5. The patterns of DBPsFP formed by six DOM fractions in Aha Reservoir upon chlorination during initial-wet periods (a. HOB; b. HIB; c. HOA; d. HIA; e. HON; f. HIN). #S1: the estuary of Jinzhong river; #S2: drinking water intake of Aha reservoir; #S3: estuary of Youyu river. (Significance level: 0.05, N = 2).

humic acid and SMP-like substances with strong FI (Fig. S2e, f and h), whereas higher TCM formation potential was observed compared to N-DBPs. N-DBP formation was mainly generated from HIN (SMP source, Fig. S2g), which probably possessed more organic nitrogen. Previous studies also indicate that precursors of haloacetonitriles (HANs) were from glutamic acid, histidine and COOH–CH$_2$–CN structure (Bond et al., 2011; Wang et al., 2013). Thus, carbonaceous DBP precursors were probably derived from terrigenous DOM, whereas a strong linkage exists between nitrogenous DBP formation and AOM at inland karst reservoir.

3.4. Influence of divalent ions on DBPsFP

DBPsFP, specific UV, and 3D-EEM intensity variations are shown in Fig. 6 under the presence of different Ca^{2+} and Mg^{2+} levels. In Fig. 6a, the TCM formation potential increased by 2.85 μg mgDOC^{-1} under the presence of 135.71 mg L^{-1} of Ca^{2+} and 18.43 mg L^{-1} Mg^{2+}, indicating that doubled levels of Ca^{2+} promoted TCM formation. For spectra analysis, enhanced divalent ion levels decreased aromatic (SUVA$_{254}$), protein (SUVA$_{280}$) and fulvic acid (SUVA$_{285}$) levels (Fig. 6b), AOM

tended to possess the characteristics of humic-like carbon (region V, Fig. 6c). Navalon et al. (2009) reported THM promotion was responsible from ligands from Ca^{2+} with polyols, citric and humic acids. Divalent ions also linked to complex functional groups (hydroxyl, carbonyl, and carboxyl of humic-like substances), showing a catalytic effect on TCM formation (Dudev and Lim, 2007; Navalon et al., 2009; Yan et al., 2015). Surprisingly, there were no discernible DCAN formation changed with the increase dosage of Ca^{2+} and Mg^{2+}, which suggested that subsequent amount variation of aromatic, fulvic and humic-like substances (Fig. 6b) merely affect N-DBP formation. HAN formation came from aspartic acid and asparagine where both shown to possess acidic and polar uncharged amino acid group, with the formation of dichlorocyanoacetic acid decarboxylated to form DCAN (Huang et al., 2012; Wang et al., 2013). Then DCAN could be formed due to the cleavage of the bond of α-carbon and amine group (Wang et al., 2013). The presence of Ca^{2+} and Mg^{2+} in karst water may enhance TCM formation by humic-like components, but not affect α-carbon and amine group structure, and thus no obvious N-DBPs were observed with the increase of divalent ions.
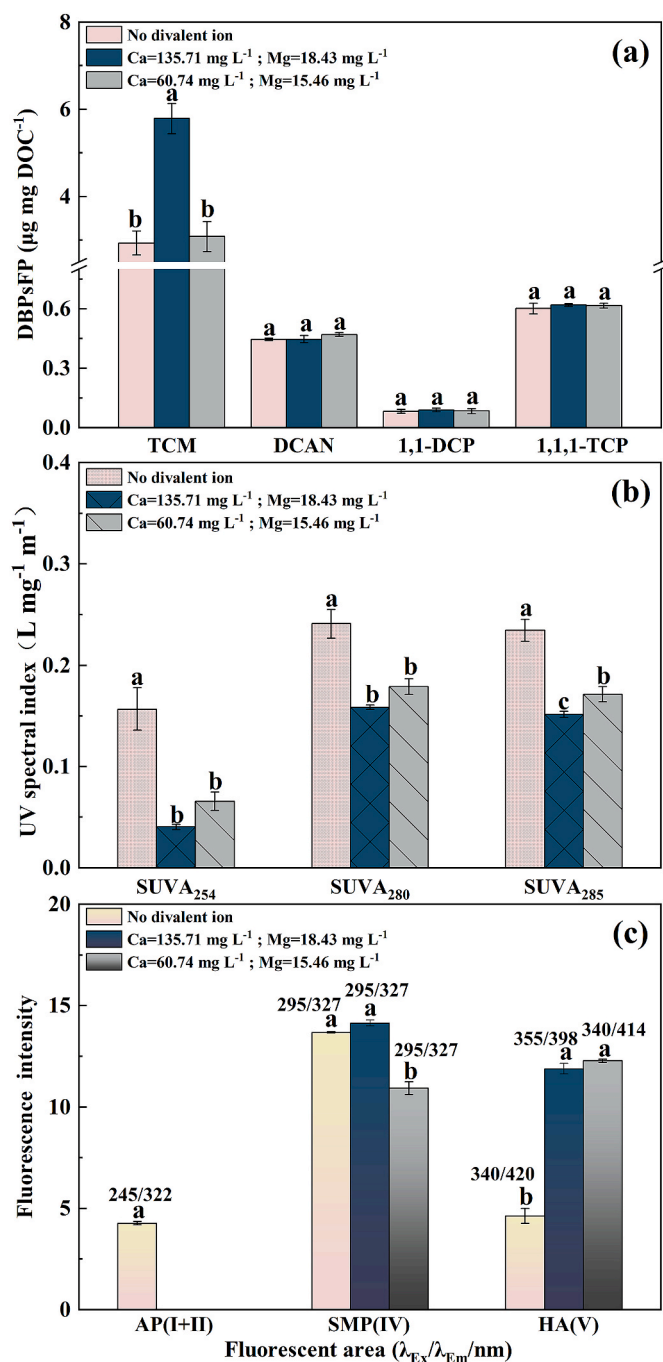
Fig. 6. The influence of Ca^{2+} and Mg^{2+} levels on DBPsFP and specific spectral (UV and fluorescence) parameters of *Chlorella* sp. AOM (a: DBPsFP of AOM extracted from *Chlorella* sp. b: UV spectral characteristics of *Chlorella* sp. AOM; c: 3D-EEM characteristic peaks of *Chlorella* sp. AOM; AP: aromatic protein; SMP: soluble microbial product; HA: humic acid, Significance level: 0.05, N = 2).

4. Conclusion

Chemical characteristics and DBP contributions from DOM and its fractions were obtained in a typical karst surface water. Both terrigenous and autochthonous DOM performed as critical DBP precursors, and DBP formation patterns were tightly correlated to DOM chemical variations. TCAN and DCAN formation were significantly higher in the drought period compared to that in the post-wet period. In addition, hydrophobic components showed higher C-DBP formation compared to hydrophilic counterparts, while hydrophilic DOM fractions may possess

abundant N-DBP precursors. The presence of Ca^{2+} and Mg^{2+} in karst water enhanced the generation of C-DBPs (TCM) but not N-DBPs (DCAN) from *Chlorella* sp. AOM. Divalent ions might be complex unsaturated functional groups in AOM as ligands. Humic-like substances produced but did not affect α-carbon and amine group structure. Monitoring terrestrial DOM input and AOM chemical characteristics might serve as a feasible approach for controlling DBP risk in karst surface water.

Credit author statement

Hui Zhou: Investigation, Data curation, Writing – original draft preparation; Liye Tian Investigation, Data curation, Writing – original draft preparation; Maofei Ni: Conceptualization, Methodology, Validation, Funding acquisition, Supervision; Sixi Zhu: Investigation, Data curation; Runyu Zhang: Supervision; Liying Wang: Data curation; Ming Wang: Validation; Zhikang Wang: Supervision, Methodology, Funding acquisition, Writing- Reviewing and Editing.

Declaration of competing interest

The authors declare that they have no known competing financial interests or personal relationships that could have appeared to influence the work reported in this paper.

Data availability

Data will be made available on request.

Acknowledgement

Appendix A. Supplementary data

Supplementary data to this article can be found online at https://doi.org/10.1016/j.chemosphere.2022.136324.

References

Aiken, G.R., Mcknight, D.M., Thorn, K.A., Thurman, E.M., 1992. Isolation of hydrophilic organic acids from water using nonionic macroporous resins. Org. Geochem. 18 (4), 567–573.

Baghoth, S.A., Sharma, S.K., Amy, G.L., 2011. Tracking natural organic matter (NOM) in a drinking water treatment plant using fluorescence excitation–emission matrices and PARAFAC. Water Res. 45 (2), 797–809.

Baird, R.B., Eaton, A.D., Rice, E.W., 2017. Standard methods for the examination of water and wastewater, 23rd edition. APHA, AWWA, WEF, Washington DC.

Bao, Q., Liu, Z., Zhao, M., Hu, Y., Zhang, Y., 2020. Primary productivity and seasonal dynamics of planktonic algae species composition in karst surface waters under different land uses. J. Hydrol. 591, 1–12.

Bond, T., Huang, J., Templeton, M.R., Graham, N., 2011. Occurrence and control of nitrogenous disinfection by-products in drinking water-A review. Water Res. 45 (15), 4341–4354.

Chang, H., Chen, C., Wang, G., 2013. Characteristics of C-, N-DBPs formation from nitrogen-enriched dissolved organic matter in raw water and treated wastewater effluent. Water Res. 47 (8), 2729–2741.

Chen, B., Yang, R., Liu, Z., Sun, H., Yan, H., Zeng, Q., Zeng, S., Zeng, C., Zhao, M., 2017. Coupled control of land uses and aquatic biological processes on the diurnal hydrochemical variations in the five ponds at the Shawan Karst Test Site, China: implications for the carbonate weathering-related carbon sink. Chem. Geol. 456, 58–71.

Chen, W., Westerhoff, P., Leenheer, J.A., Booksh, K., 2003. Fluorescence excitation-emission matrix regional integration to quantify spectra for dissolved organic matter. Environ. Sci. Technol. 37 (24), 5701–5710.

Cuny, P., Marty, J.C., Chiavérini, J., Vescovali, I., Raphel, D., Rontani, J.F., 2002. One-year seasonal survey of the chlorophyll photodegradation process in the northwestern Mediterranean Sea. Deep Sea Res. Part II Top. Stud. Oceanogr. 49 (11), 1987–2005.

Deng, L.J., Ngo, H.H., Guo, W., Zhang, H.W., 2019. Pre-coagulation coupled with sponge-membrane filtration for organic matter removal and membrane fouling control during drinking water treatment. Water Res. 157, 155–166.

Dudev, T., Lim, C., 2007. Effect of carboxylate-binding mode on metal binding/selectivity and function in proteins. Acc. Chem. Res. 40 (1), 85–93.

Fichot, C., Benner, R., 2012. The spectral slope coefficient of chromophoric dissolved organic matter (S275–295) as a tracer of terrigenous dissolved organic carbon in river-influenced ocean margins. Limnol. Oceanogr. 57, 1453–1466.

Ge, Q., Zhang, P., Ni, M., Guo, Y., Wang, Z., Hui, Z., Zhang, Z., Zhou, Y., 2021. Relationships between phytoplankton and environmental factors in a typical karst plateau reservoir. Ecology and Environmental Sciences 30 (1), 156–164.

Goslan, E.H., Seigle, C., Purcell, D., Henderson, R., Parsons, S.A., Jefferson, B., Judd, S.J., 2017. Carbonaceous and nitrogenous disinfection by-product formation from algal organic matter. Chemosphere 170, 1–9.

Gu, X., Zhai, H.Y., Zhou, Y.A., 2020. formation of disinfection byproducts from algal organic matter exposed to monochloramine: effects of monochloramine dosages, pH, and bromide concentrations. Water, Air, Soil Pollut. 231 (5), 207–219.

Han, J.R., Zhang, X.R., Jiang, J.Y., Li, W.X., 2021. How much of the total organic halogen and developmental toxicity of chlorinated drinking water might be attributed to aromatic halogenated DBPs? Environ. Sci. Technol. 55 (9), 5906–5916.

Hansen, A.M., Kraus, T.E.C., Pellerin, B.A., Fleck, J.A., Downing, B.D., Bergamaschi, B.A., 2016. Optical properties of dissolved organic matter (DOM): effects of biological and photolytic degradation. Limnol. Oceanogr. 61 (3), 1015–1032.

Helms, J.R., Stubbins, A., Ritchie, J.D., Minor, E.C., Kieber, D.J., Mopper, K., 2008. Absorption spectral slopes and slope ratios as indicators of molecular weight, source, and photobleaching of chromophoric dissolved organic matter. Limnol. Oceanogr. 53, 955–969.

Holroyde, M.J., Robertson, S.P., Johnson, J.D., Solaro, R.J., Potter, J.D., 1980. The calcium and magnesium binding sites on cardiac troponin and their role in the regulation of myofibrillar adenosine triphosphatase. J. Biol. Chem. 255 (24), 11688–11693.

Hua, G., Reckhow, D.A., 2007a. Comparison of disinfection byproduct formation from chlorine and alternative disinfectants. Water Res. 41 (8), 1667–1678.

Hua, G.H., Reckhow, D.A., 2007b. Characterization of disinfection byproduct precursors based on hydrophobicity and molecular size. Environ. Sci. Technol. 41 (9), 3309–3315.

Huang, H., Wu, Q.Y., Hu, H.Y., Mitch, W.A., 2012. Dichloroacetonitrile and dichloroacetamide can form independently during chlorination and chloramination of drinking waters, model organic matters, and wastewater effluents. Environ. Sci. Technol. 46 (19), 10624–10631.

Jiang, J.Y., Han, J.R., Zhang, X.R., 2020. Nonhalogenated aromatic DBPs in drinking water chlorination: a gap between NOM and halogenated aromatic DBPs. Environ. Sci. Technol. 54 (3), 1646–1656.

Karimova, F.G., Kortchouganova, E.E., Tarchevsky, I.A., Iagoucheva, M.R., 2000. The oppositely directed Ca^{2+} and Na$^+$ transmembrane transport in algal cells. Protoplasma 213 (1), 93–98.

Kida, M., Fujitake, N., Suchewaboripont, V., Poungparn, S., Tomotsune, M., Kondo, M., Yoshitake, S., Iimura, Y., Kinjo, K., Maknual, C., 2018. Contribution of humic substances to dissolved organic matter optical properties and iron mobilization. Aquat. Sci. 80 (3), 26–37.

Kida, M., Kojima, T., Tanabe, Y., Hayashi, K., Kudoh, S., Maie, N., Fujitake, N., 2019. Origin, distributions, and environmental significance of ubiquitous humic-like fluorophores in Antarctic lakes and streams. Water Res. 163, 1–11.

Lee, M.H., Osburn, C.L., Shin, K.H., Hur, J., 2018. New insight into the applicability of spectroscopic indices for dissolved organic matter (DOM) source discrimination in aquatic systems affected by biogeochemical processes. Water Res. 147, 164–176.

Leenheer, J.A., 1981. Comprehensive approach to preparative isolation and fractionation of dissolved organic carbon from natural waters and wastewaters. Environ. Sci. Technol. 15 (5), 578–587.

Leloup, M., Nicolau, R., Pallier, V., Yéprémian, C., Feuillade-Cathalifaud, G., 2013. Organic matter produced by algae and cyanobacteria: quantitative and qualitative characterization. J. Environ. Sci. 25 (6), 1089–1097.

Li, L.L., Jiang, T., Yan, J.L., Guo, N., Wei, S.Q., Wang, D.Y., Gao, J., Zhao, Z., 2014. Ultraviolet-visible (UV–Vis) spectral characteristics of dissolved organic matter (DOM) in soils and sediments of typical water-level fluctuation zones of three gorges reservoir areas. Environ. Sci. J. Integr. Environ. Res. 35 (3), 933–941.

Li, X., Rao, N.R.H., Linge, K.L., Joll, C.A., Khan, S., Henderson, R.K., 2020. Formation of algal-derived nitrogenous disinfection by-products during chlorination and chloramination. Water Res. 183, 1–14.

Liang, L., Singer, P.C., 2003. Factors influencing the formation and relative distribution of haloacetic acids and trihalomethanes in drinking water. Environ. Sci. Technol. 37 (13), 2920–2928.

Liu, W., Tanaka, L., Liu, P., Qin, X., Shan, X., Yao, X., 2018. FDOM conversion in karst watersheds expressed by three-dimensional fluorescence spectroscopy. Water 10 (10), 1–18.

Liu, Z., Dreybrodt, W., 2015. Significance of the carbon sink produced by H$_2$O–carbonate–CO$_2$–aquatic phototroph interaction on land. Sci. Bull. 60 (2), 182–191.

Longyang, Q.Q., 2019. Assessing the effects of climate change on water quality of plateau deep-water lake-A study case of Hongfeng Lake. Sci. Total Environ. 647, 1518–1530.

Lu, X.X., Li, S.Y., He, M., Zhou, Y., Bei, R.T., Li, L., Ziegler, A., 2011. Seasonal changes of nutrient fluxes in the Upper Changjiang basin: an example of the Longchuanjiang River, China. J. Hydrol. 405 (3), 344–351.

Melcrová, A., Pokorna, S., Vošahlíková, M., Sýkora, J., Svoboda, P., Hof, M., Cwiklik, L., Jurkiewicz, P., 2019. Concurrent compression of phospholipid membranes by calcium and cholesterol. Langmuir 35 (35), 11358–11368.

Navalon, S., Alvaro, M., Garcia, H., 2009. Ca^{2+} and Mg^{2+} present in hard waters enhance trihalomethane formation. J. Hazard Mater. 169 (1–3), 901–906.

Ni, M.F., Ge, Q.S., Li, S.Y., Wang, Z.K., Wu, Y.J., 2021. Trophic state index linked to partial pressure of aquatic carbon dioxide in a typical karst plateau lake. Ecol. Indicat. 120, 1–11.

Ni, M.F., Jiang, S.H., Li, S.Y., 2020. Spectroscopic indices trace spatiotemporal variability of dissolved organic matter in a river system with Karst characteristic. J. Hydrol. 590, 1–10.

Ni, M.F., Zhou, H., Ma, Y.M., Su, Y., Wang, X.D., Wang, Z.K., 2022. Dissolved organic matter component and source characteristics of the metropolitan lakes and reservoirs in a typical karst region. Environ. Sci. J. Integr. Environ. Res. 43 (7), 3552–3561.

O'Driscoll, C., Mcgillicuddy, E., Croot, P., Bartley, P., Morrison, L., 2020. Tracing sources of natural organic matter, trihalomethanes and metals in groundwater from a karst region. Environ. Sci. Pollut. Control Ser. 27 (9), 12587–12600.

Omanović, D., Santinelli, C., Marcinek, S., Gonnelli, M., 2019. ASFit-An all-inclusive tool for analysis of UV-Vis spectra of colored dissolved organic matter (CDOM). Comput. Geosci. 133, 1–9.

Pápista, É., Ács, É., Böddi, B., 2002. Chlorophyll-a determination with ethanol-a critical test. Hydrobiologia 485 (1), 191–198.

Pavlis, M., Cummins, E., 2014. Using total organic carbon for the assessment of groundwater vulnerability in karst regions at regional scales. Environ. Earth Sci. 72 (6), 1993–2007.

Piirsoo, K., Viik, M., Kõiv, T., Käiro, K., Laas, A., Nõges, T., Pall, P., Selberg, A., Toomsalu, L., Vilbaste, S., 2012. Characteristics of dissolved organic matter in the inflows and in the outflow of Lake Vortsjarv, Estonia. J. Hydrol. 475, 306–313.

Pivokonsky, M., Kopecka, I., Cermakova, L., Fialova, K., Novotna, K., Cajthaml, T., Henderson, R.K., Pivokonska, L., 2021. Current knowledge in the field of algal organic matter adsorption onto activated carbon in drinking water treatment. Sci. Total Environ. 799, 1–19.

Pivokonsky, M., Naceradska, J., Kopecka, I., Baresova, M., Jefferson, B., Li, X., Henderson, R.K., 2015. The impact of algogenic organic matter on water treatment plant operation and water quality: a review. Crit. Rev. Environ. Sci. Technol. 46 (4), 291–335.

Pokharel, R., Gerrits, R., Schuessler, J.A., Frings, P.J., Sobotka, R., Gorbushina, A.A., von Blanckenburg, F., 2018. Magnesium stable Isotope fractionation on a cellular level explored by cyanobacteria and black fungi with Implications for higher plants. Environ. Sci. Technol. 52 (21), 12216–12224.

Richardson, S.D., Plewa, M.J., Wagner, E.D., Schoeny, R., DeMarini, D.M., 2007. Occurrence, genotoxicity, and carcinogenicity of regulated and emerging disinfection by-products in drinking water: a review and roadmap for research. Mutat. Res. Rev. Mutat. Res. 636 (1), 178–242.

Shan, J., Hu, J., Sule Kaplan-Bekaroglu, S., Song, H., Karanfil, T., 2012. The effects of pH, bromide and nitrite on halonitromethane and trihalomethane formation from amino acids and amino sugars. Chemosphere 86 (4), 323–328.

Shank, G.C., Evans, A., 2011. Distribution and photoreactivity of chromophoric dissolved organic matter in northern Gulf of Mexico shelf waters. Continent. Shelf Res. 31 (10), 1128–1139.

Song, X.W., Gao, Y., Wen, X.F., Guo, D.L., Yu, G.R., He, N.P., Zhang, J.Z., 2017. Carbon sequestration potential and its eco-service function in the karst area, China. J. Geogr. Sci. 27 (8), 967–980.

Stedmon, C.A., Bro, R., 2008. Characterizing dissolved organic matter fluorescence with parallel factor analysis: a tutorial. Limnol Oceanogr. Methods 6 (11), 572–579.

Sururi, M., Notodarmojo, S., Roosmini, D., Putra, P., Maulana, Y., Dirgawati, M., 2020. An investigation of a conventional water treatment plant in reducing dissolved organic matter and trihalomethane formation potential from a tropical river water source. J. Eng. Technol. Sci. 52 (2), 271–288.

Tedetti, M., Longhitano, R., Garcia, N., Guigue, C., Ferretto, N., Goutx, M., 2012. Fluorescence properties of dissolved organic matter in coastal Mediterranean waters influenced by a municipal sewage effluent (Bay of Marseilles, France). Environ. Chem. 9 (5), 438–449.

Waditee, R., Hossain, G.S., Tanaka, Y., Nakamura, T., Shikata, M., Takano, J., Takabe, T., Takabe, T., 2004. Isolation and functional characterization of Ca^{2+}/H$^+$ antiporters from cyanobacteria. J. Biol. Chem. 279 (6), 4330–4338.

Wagner, E.D., Plewa, M.J., 2017. CHO cell cytotoxicity and genotoxicity analyses of disinfection by-products: an updated review. J. Environ. Sci. 58, 64–76.

Wang, L.Y., Wu, F.C., Zhang, R.Y., Li, W., Liao, H.Q., 2009. Characterization of dissolved organic matter fractions from Lake Hongfeng, southwestern China Plateau. J. Environ. Sci. 21 (5), 581–588.

Wang, X.P., Zhang, F., Kung, H.T., Ghulam, A., Trumbo, A.L., Yang, J.Y., Ren, Y., Jing, Y.Q., 2017. Evaluation and estimation of surface water quality in an arid region based on EEM-PARAFAC and 3D fluorescence spectral index: a case study of the Ebinur Lake Watershed, China. Catena 155, 62–74.

Wang, X.X., Liu, B.M., Lu, M.F., Li, Y.P., Jiang, Y.Y., Zhao, M.X., Huang, Z.X., Pan, Y., Miao, H.F., Ruan, W.Q., 2021. Characterization of algal organic matter as precursors for carbonaceous and nitrogenous disinfection byproducts formation: comparison with natural organic matter. J. Environ. Manag. 282, 111951.

Wang, Z.K., Choi, O., Seo, Y.Y., 2013. Relative contribution of biomolecules in bacterial extracellular polymeric substances to disinfection by-product formation. Environ. Sci. Technol. 47 (17), 9764–9773.

Wang, Z.K., Hessler, C.M., Xue, Z., Seo, Y., 2012a. The role of extracellular polymeric substances on the sorption of natural organic matter. Water Res. 46 (4), 1052–1060.

Wang, Z.K., Kim, J., Seo, Y., 2012b. Influence of bacterial extracellular polymeric substances on the formation of carbonaceous and nitrogenous disinfection byproducts. Environ. Sci. Technol. 46 (20), 11361–11369.

Waterson, E.J., Canuel, E.A., 2008. Sources of sedimentary organic matter in the Mississippi River and adjacent Gulf of Mexico as revealed by lipid biomarker and δ^{13}C-TOC analyses. Org. Geochem. 39 (4), 422–439.

Xu, F.C., Yao, Y.X., Alvarez, P.J.J., Li, Q.L., Fu, H.Y., Yin, D.Q., Zhu, D.Q., Qu, X.L., 2019. Specific ion effects on the aggregation behavior of aquatic natural organic matter. J. Colloid Interface Sci. 556, 734–742.

Xu, X.T., Kang, J., Shen, J.M., Zhao, S.X., Wang, B.Y., Zhang, X.X., Chen, Z.L., 2021. EEM-PARAFAC characterization of dissolved organic matter and its relationship with disinfection by-products formation potential in drinking water sources of northeastern China. Sci. Total Environ. 774, 1–9.

Yan, M.Q., Lu, Y.J., Gao, Y., Benedetti, M.F., Korshin, G.V., 2015. In-situ investigation of interactions between magnesium Ion and natural organic matter. Environ. Sci. Technol. 49 (14), 8323–8329.

Yang, M.T., Zhang, X.R., 2013. Comparative developmental toxicity of new aromatic halogenated DBPs in a chlorinated saline sewage effluent to the marine polychaete *Platynereis dumerilii*. Environ. Sci. Technol. 47 (19), 10868–10876.

Yang, M.T., Zhang, X.R., Liang, Q.H., Yang, B., 2019. Application of LC/MS/MS precursor ion scan for evaluating the occurrence, formation and control of polar halogenated DBPs in disinfected waters: a review. Water Res. 158, 322–337.

Yang, M.X., Liu, Z.H., Sun, H.L., Yang, R., Chen, B., 2017. Organic carbon source tracing and DIC fertilization effect in the Pearl River: insights from lipid biomarker. Earth Environ. 45 (1), 46–56.

Yuan, F.S., Quellos, J.A., Fan, C.J., 2013. Controls of phosphorus loading and transport in the Cuyahoga River of northeastern Ohio, USA. Appl. Geochem. 38, 59–69.

Zhang, R.Y., Wang, L.Y., Chen, J.A., 2021. Sources and selective preservation of organic matter in the karst watershed: evidence from sediment records in a plateau deep lake, Southwestern China. Environ. Sci. Pollut. Control Ser. 28 (4), 4762–4777.

Zhao, Y., Yang, H.W., Liu, S.T., Tang, S., Wang, X.M., Xie, Y.F.F., 2016. Effects of metal ions on disinfection byproduct formation during chlorination of natural organic matter and surrogates. Chemosphere 144, 1074–1082.

Zheng, L.C., Song, Z.F., Meng, P.P., Fang, Z.Q., 2016. Seasonal characterization and identification of dissolved organic matter (DOM) in the Pearl River, China. Environ. Sci. Pollut. Control Ser. 23 (8), 7462–7469.

Zhou, X.R., Lin, Y.L., Zhang, T.Y., Xu, B., Chu, W.H., Cao, T.C., Zhu, W.Q., 2019. Speciation and seasonal variation of various disinfection by-products in a full-scale drinking water treatment plant in East China. Water Sci. Technol. Water Supply 19, 1579–1586.